



Measurement of Thermal Conductivity of Suspended MoS₂ and MoSe₂ by Nanosecond ET-Raman Free of Temperature Calibration and Laser Absorption Evaluation

Journal:	<i>Nanoscale</i>
Manuscript ID	NR-ART-07-2018-005641.R2
Article Type:	Paper
Date Submitted by the Author:	11-Nov-2018
Complete List of Authors:	Wang, Ridong; Iowa State University, Mechanical Engr. Wang, Tianyu; Iowa State University Zobeiri, Hamidreza; Iowa State University, Mechanical Engr. Yuan, Pengyu; E O Lawrence Berkeley National Laboratory Deng, Cheng; Tianhe College of Guangdong Polytechnic Normal University Yue, Yanan; Wuhan University, School of Power and Mechanical Engineering Xu, Shen; Shanghai University of Engineering Science Wang, Xinwei; Iowa State University, Mechanical Engr.

Measurement of Thermal Conductivity of Suspended MoS₂ and MoSe₂ by Nanosecond ET-Raman Free of Temperature Calibration and Laser Absorption Evaluation

Ridong Wang,[†] Tianyu Wang,[†] Hamidreza Zobeiri,[†] Pengyu Yuan,[‡] Cheng Deng,[#]

Yanan Yue,⁺ Shen Xu,^{*§} Xinwei Wang^{*†}

[†] Department of Mechanical Engineering, Iowa State University, Ames, Iowa 50011, United States.

[‡] The Molecular Foundry, Lawrence Berkeley National Laboratory, One Cyclotron Road, Building 67, Berkeley, CA 94720, United States.

[#] College of Mechatronics Engineering, Guangdong Polytechnic Normal University, Guangzhou 510635, People's Republic of China.

⁺ School of Power and Mechanical Engineering, Wuhan University, Wuhan 430072, People's Republic of China.

[§] Automotive Engineering College, Shanghai University of Engineering Science, 333 Longteng Road, Shanghai 201620, People's Republic of China.

Abstract: Steady state Raman spectroscopy is the most widely used opto-thermal technique for measuring 2D atomic-layer material's thermal conductivity. It requires calibration of temperature coefficients of Raman properties and measurement/calculation of the absolute laser absorption in 2D materials. Such requirement is very laborious and introduces very large measurement errors (in the order of 100%) and hinders precise and deep understanding of phonon-structure interaction in 2D materials. In this work, a novel nanosecond energy transport state resolved Raman (ns ET-Raman) technique is developed to resolve those critical issues and achieve

unprecedented measurement precision, accuracy and ease of implementation. In ns ET-Raman, two energy transport states are constructed: steady state and nanosecond thermal transport and Raman probing. The ratio of temperature rise under the two states eliminates the need of Raman temperature calibration and laser absorption evaluation. Four suspended MoS₂ (45 – 115 nm thick) and four suspended MoSe₂ (45 – 140 nm thick) samples are measured and compared using ns ET-Raman. With the increased sample thickness, the measured thermal conductivity increases from 40.0 ± 2.2 to 74.3 ± 3.2 W·m⁻¹·K⁻¹ for MoS₂, and from 11.1 ± 0.4 to 20.3 ± 0.9 W·m⁻¹·K⁻¹ for MoSe₂. This is attributed to the decreased significance of surface phonon scattering in thicker samples. The ns ET-Raman features up-to-date most advanced capability for measuring the thermal conductivity of 2D materials and will find broad applications in studying low-dimensional materials.

Keywords: in-plane thermal conductivity, 2D atomic-layer materials, Raman spectroscopy, nanosecond laser, energy transport states

▪ Introduction

2D atomic-layer materials such as graphene,¹⁻² hexagonal boron nitride (h-BN),³ black phosphorus,^{4, 5} molybdenum disulfide (MoS₂),⁶ and molybdenum diselenide (MoSe₂)⁷ have attracted significant research interest. One of the reasons for the rapid progress is that these materials are thought to be the most suitable candidates to eventually create a new generation of electronic devices.^{8, 9} And the performance of electronic devices largely relies on the heat dissipation property and hence on the thermal conductivity of the materials.¹⁰ As a result, it is very crucial to measure, understand, and tailor/improve the thermal conductivity of 2D atomic-layer materials.

Some previous studies have reported the thermal conductivity of different 2D atomic-layer materials. Jo *et al.*¹¹ used a microbridge device with built-in resistance thermometers to measure the thermal conductivity of suspended few-layered hexagonal boron nitride (h-BN). Based on the obtained thermal resistance of the 11-layer h-BN samples with suspended lengths ranging from 3 to 7.5 μm , the in-plane thermal conductivity under room temperature was measured to be about $360 \text{ W}\cdot\text{m}^{-1}\cdot\text{K}^{-1}$. In this method, the measurement accuracy is jeopardized by the unknown thermal contact resistance between the sample and the contacts. Jang *et al.*¹² measured the thermal conductivity in different directions of mechanically exfoliated black phosphorus (BP) of 138 – 552 nm thickness using the conventional time-domain thermoreflectance (TDTR) and beam-offset TDTR method. The highest in-plane thermal conductivities were 86 ± 8 and $34 \pm 4 \text{ W}\cdot\text{m}^{-1}\cdot\text{K}^{-1}$ along the zigzag and the armchair directions, respectively. And the cross-plane thermal conductivity was $4.0 \pm 0.5 \text{ W}\cdot\text{m}^{-1}\cdot\text{K}^{-1}$. Compared with other methods, this method requires more complicated setups and very careful operation to obtain data for further analysis.¹³

Shahil *et al.*¹⁴ used the transient “laser flash” technique (LFT) to measure the cross-plane thermal conductivity of graphene-based thermal interface materials. Based on the resulting temperature evolution, the thermal diffusivity could be determined. The specific heat of the material could be obtained by comparing the magnitude of the temperature rise to that of reference calibration sample. Then, the thermal conductivity was calculated by using these two parameters. However, this method cannot be used to measure thin films. Typical commercial laser flash instruments can measure samples with a thickness of $\sim 100 \mu\text{m}$ and above depending on the thermal diffusivity of the sample.¹⁵

Among the different methods to measure the thermal properties of 2D atomic-layer materials, an optothermal method based on Raman spectroscopy is the most widely used one.¹⁶ In this method, a laser is focused on the 2D atomic-layer material and the positions of the corresponding Raman-active mode are measured. The laser heating enables Raman red-shift due to thermal softening.¹⁷ Thermal modeling can then be used to extract the thermal conductivity from the measured shift rate. Several parameters, such as the rate of mode softening with temperature,¹⁸ optical absorption,¹⁹ 2D atomic layer interface thermal resistance (R),²⁰ and hot carrier diffusion coefficient (D)²¹ are required to realize the determination of thermal conductivity using the thermal modeling. The work by Yuan *et al.*²¹ is the first one to consider the energy redistribution by hot carriers and they were able to measure the hot carrier diffusivity and mobility via a completely non-contact way.

As the optothermal method based on Raman spectroscopy is a widely used method, many research groups used this method to measure the thermal conductivity of 2D atomic-layer

materials. Lee *et al.*²² measured the thermal conductivity of suspended pristine graphene over holes with diameter ranging from 2.6 to 6.6 μm . Luo *et al.*²³ reported the anisotropic in-plane thermal conductivity of suspended few-layered BP. Yan *et al.*²⁴ used this technique to measure the thermal conductivity of suspended monolayer MoS_2 over holes with a diameter of 1.2 μm . Zhang *et al.*²⁵ used this technique to study the thermal conductivity of monolayer and bilayer MoS_2 , monolayer and bilayer MoSe_2 . To minimize the effects of the finite spot size, the samples were suspended over holes with diameter between 2.5 and 5 μm .

Though the optothermal method based on Raman spectroscopy has been widely used to measure the thermal conductivity of 2D atomic-layer materials, a significant drawback of this method is that both temperature and power dependent Raman study should be done to extract the thermal conductivity of the sample. However, the temperature-dependent Raman study is very time consuming and could introduce large errors. Also the laser absorption is subject to very large errors induced by unknown sample-to-sample optical property variation. In our recently published work, we have developed a novel and more advanced technique: energy transport state-resolved Raman (ET-Raman) to study the 2D atomic-layer materials' thermal properties.²⁶ The error introduced by Raman property temperature coefficient calibration could be eliminated using this technique. The ET-Raman is based on two extreme energy transport situations: near zero-transport using a picosecond (ps) laser Raman and steady-state using a continuous-wave (CW) laser Raman. One of the most attractive perspectives is that we do not need to know the laser absorption coefficient or the temperature coefficients of the Raman properties. The hot carrier diffusivity and interface thermal resistance could be determined by just comparing the Raman shift variation measured from different energy transport states in time and space domains.

Thus, this technique eliminates the errors brought in by local optical absorption evaluation, temperature coefficient calibration, and the effects from electrical contact used in carrier mobility measurement. However, this ET-Raman technique with a picosecond laser can only be used for supported materials since the pulse interval is so short that a strong heat accumulation for suspended 2D atomic-layer materials will happen.

In this work, we conduct further development of the ET-Raman technique using a nanosecond (ns) laser for measuring the thermal conductivity of suspended 2D atomic-layer materials. The pulse interval of the ns laser is 10 μ s, which is much longer than that of the ps laser (\sim 26 ns). A ns ET-Raman technology is developed to measure the in-plane thermal conductivity of suspended MoS₂ and MoSe₂. The thickness effect on in-plane thermal conductivity for these two 2D atomic-layer materials is explored. The thickness of the nanosheets ranges from 45 nm to 115 nm for MoS₂, and from 40 nm to 135 nm for MoSe₂.

▪ Results and Discussion

ns ET-Raman Physics. Although the Raman active optical phonons do not play a significant role in directly conducting heat in the in-plane direction, their frequency of vibration is reasonably sensitive to the local temperature fluctuations caused by external effects.²⁷ The temperature increase of the suspended sample under laser excitation is directly related to the thermal conductivity of the material.²⁸ In the ns ET-Raman technique, we construct two distinct energy transport states in time domain to probe the materials' thermal response. Two lasers with 532 nm wavelength are used to irradiate the samples for both laser heating and Raman probing. Figure 1(a) shows the suspended sample, and the center of sample is irradiated by the laser. The

first energy transport state is the steady-state heating. As shown in Figure 1(b) and (c), a CW laser is used to generate steady-state heating, and to explore the temperature profile that depends on thermal conductivity. The MoS₂ or MoSe₂ nanosheets will absorb the laser energy and transport it along the in-plane and cross-plane directions. Compared with its lateral size, the thickness of the nanosheets is very small. As a result, the energy transport in the cross-plane direction could be neglected and the temperature can be treated constant in the thickness direction. Raman signal is also excited during the laser heating and could be collected to obtain the temperature profile of the sample. By using different laser powers (P), a parameter called Raman shift power coefficient (RSC) could be obtained: $\psi_{\text{CW}} = \partial\omega / \partial P = \alpha (\partial\omega / \partial T) f_1(\kappa)$. ψ_{CW} is determined by laser absorption coefficient (α), temperature coefficient of Raman shift ($\partial\omega / \partial T$), and the in-plane thermal conductivity of the sample (κ).

The second energy transport state is opposite to the steady state: it has nearly zero transport. Figure 1(d) and (e) show that a ns laser is focused in the center of the suspended sample to realize localized heating and Raman probing. In the same way, as shown in Figure 1(f), the RSC for this ns laser heating case could also be obtained: $\psi_{\text{ns}} = \partial\omega / \partial P = \alpha (\partial\omega / \partial T) f_2(\kappa, \rho c_p)$. ψ_{ns} is determined by laser absorption coefficient, temperature coefficient of Raman shift, volumetric heat capacity (ρc_p), and the in-plane thermal conductivity of the sample. However, the thermal diffusion length from the heating region in this state is much smaller than steady state. That is, the contribution of heat conduction, which is highly related to the in-plane thermal conductivity of the sample, to the two Raman shift power coefficients are different for the two cases.

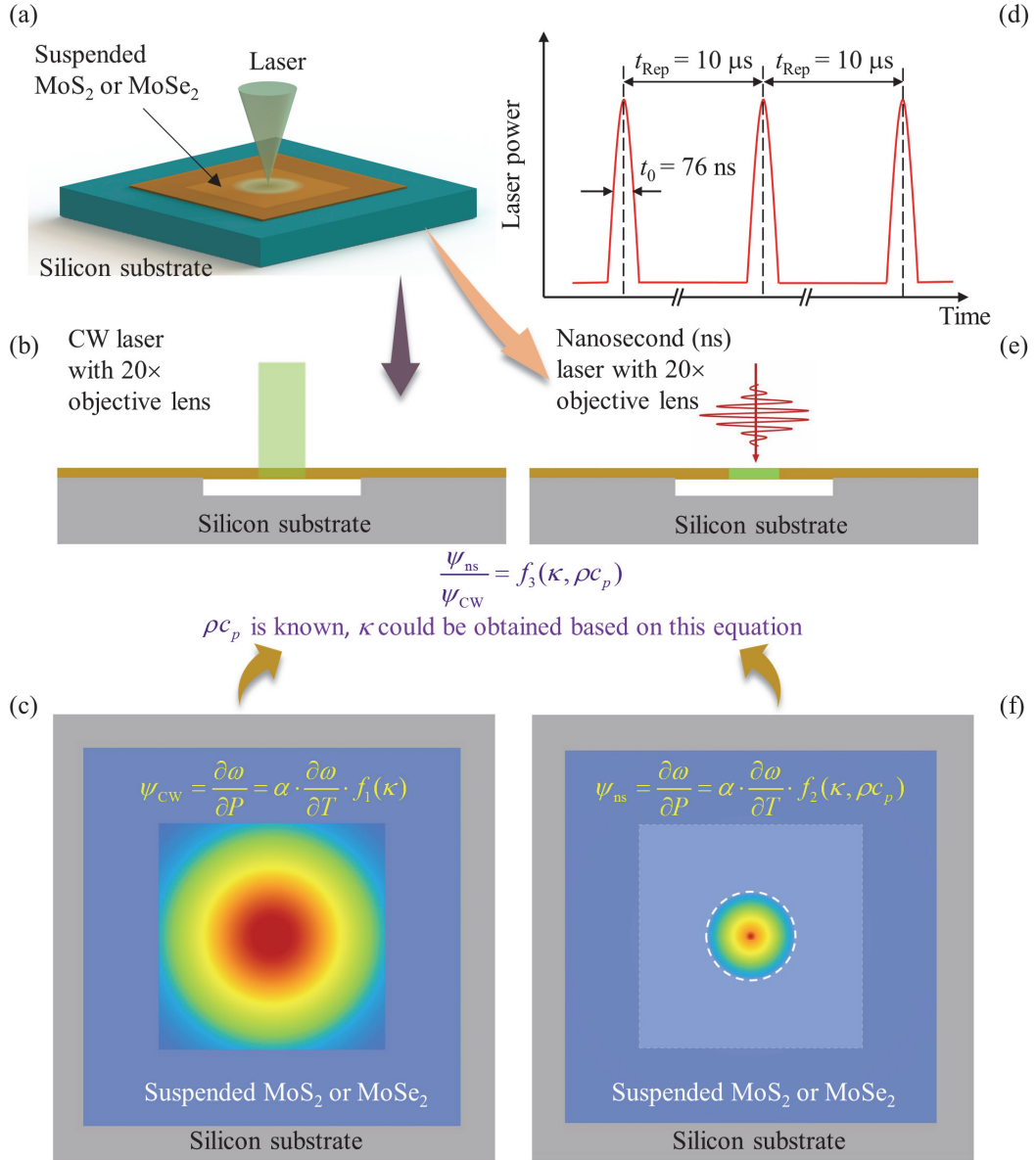


Figure 1. Illustration of the nanosecond energy transport state resolved Raman (ns ET-Raman) concept. (a) The MoS₂ or MoSe₂ nanosheets are transferred to the silicon substrate with a hole beneath. (b)-(f) A 532 nm continuous-wave (CW) laser and a 532nm nanosecond (ns) laser are used to generate two different energy transport states in the time domain with the same objective lens (20×). Due to the different contribution of in-plane thermal conductivity under the two energy transport states, the in-plane thermal conductivity of the sample could be obtained.

Based on these two Raman shift power coefficients, a dimensionless normalized RSC is defined as $\Theta = \psi_{\text{ns}} / \psi_{\text{CW}} = f_3(\kappa, \rho c_p)$. Although ψ_{CW} and ψ_{ns} are all influenced by laser absorption

coefficient and temperature coefficient of Raman shift, the effect of these two parameters are completely ruled out in this normalized RSC. The laser power used in the experiments is very low, so that the temperature rise of the sample is moderate. In our work, the volumetric heat capacity of the sample has negligible size effect and shares the same value of the bulk counterpart. Then, Θ is only related to the unknown in-plane thermal conductivity of the sample. Due to the different contribution of heat conduction under the two energy transport states, this normalized RSC could be used to obtain the in-plane thermal conductivity of the samples of different thickness. A 3D heat conduction model is used to simulate the temperature rise under the two energy transport states. Then, a relationship between the temperature rise ratio of the two energy transport states and the in-plane thermal conductivity of the sample could be built. And the in-plane thermal conductivity of the samples with different thickness could be finally determined based on the measured Θ .

For the steady-state heating, the energy transport in the sample is governed by the differential equation^{21,22} as below:

$$\kappa \nabla^2 T_{cw} + \dot{q} = 0 \quad (1)$$

where T_{cw} (K) is the temperature rise in steady-state heating, r radial position from the center of the hole, κ ($\text{W}\cdot\text{m}^{-1}\cdot\text{K}^{-1}$) the in-plane thermal conductivity of the sample, \dot{q} volumetric Gaussian beam heating and is given as

$$\dot{q}(r, z) = \frac{I_0}{\tau_L} \exp\left(-\frac{r^2}{r_0^2}\right) \exp\left(-\frac{z}{\tau_L}\right) \quad (2)$$

where $I_0 = P / \pi r_0^2$ is the laser power per unit area at the center of laser spot, r_0 (μm) the radius of the ns laser spot, τ_L the laser absorption depth and could be obtained based on the equation

$\tau_L = \lambda / (4\pi k_L)$,²⁹ where λ (532 nm) is the laser wavelength, k_L the extinction coefficient of the sample. We have τ_L (MoS₂) = 36.5 nm and τ_L (MoSe₂) = 20.6 nm.^{30, 31} Note that although we use this parameter for data processing in our work, any error carried in it will have negligible effect in the final determined κ .

For the transient-state heating, the width of the ns laser pulse is 76 ns, and the interval between two pulses is 10 μ s. When the laser irradiates the sample, electrons will be excited to the conduction band with holes left in the valence band. Then hot carriers (hot electrons and holes) are formed due to the higher energies compared to the Fermi Energy. The life time of these hot carriers is about nanoseconds or shorter, which is much shorter than the laser pulse width. If the hot carrier life time is longer than or comparable to the laser pulse width, the effect of the hot carrier should be considered. The equation below can be used to determine the carrier concentration $\Delta N(r, t)$ ³²:

$$\frac{\partial \Delta N}{\partial t} = D \nabla^2 \Delta N - \frac{\Delta N}{\tau} + \frac{\partial n_0}{\partial T} \frac{\partial T}{\tau} + \Phi \beta \quad (3)$$

where D , τ , and Φ are the carrier diffusion coefficient, the electron-hole recombination time and the incident photon flux of the laser source. β and n_0 are the optical laser absorption coefficient of the material and the equilibrium free-carrier density at temperature T . This also indicates that it is very important to select an appropriate laser pulse width in the experiment. In addition to the hot carrier life time, the time to reach a thermal equilibrium for the material should also be considered. This time can be estimated as $t \sim d^2 / \alpha$, where d and α are the diameter of laser spot and the thermal diffusivity of the material. The laser pulse width should be comparable to, or shorter than this time. For materials with a very small α , this time will be very

long, and a microsecond pulsed laser may also be useful. While for materials with a very large α , this time will be very short, and a picosecond pulsed laser may be needed.

For pulsed laser heating, the effective thermal diffusion length (L_d) could be estimated as $L_d = 2\sqrt{t \cdot \kappa / \rho c_p}$,³³ where ρc_p ($\text{J} \cdot \text{m}^{-3} \cdot \text{K}^{-1}$), t (s) are the volumetric heat capacity of the sample and laser pulse width. The diffusion length values of MoS₂ and MoSe₂ are about 4 and 3 μm , respectively. Note this length is much longer than the sample thickness (around 100 nm or less). Thus, it is physically reasonable to assume the sample has uniform temperature distribution in the thickness direction and this has been observed in our 3D modeling. The size of the suspended area is $22 \mu\text{m} \times 22 \mu\text{m}$. As a result, the thermal diffusion area under this state is much smaller than the sample size. A characteristic time (t_c) is used to define the time needed for the temperature to cool down to the ambient temperature after the nanosecond pulse heating. This time is estimated as $t_c = 0.2026 \rho c_p L^2 / \kappa$, where L (m) is the distance between the center of the suspended sample to the boundary of the suspended sample, which is 11 μm in our experiments. Due to the smaller thermal conductivity of MoSe₂, its corresponding characteristic time is longer, which is about 4 μs . That is, the time interval between two pulses (10 μs) is long enough for the sample to cool down to the ambient temperature for MoS₂ and MoSe₂ after a ns pulse heating. Therefore, it is confirmed that the ns pulses do not have interference with each other and no steady-state heat accumulation exists in the ns laser heating case. The Fourier equation governing the nanosecond laser heating pulse can be written as:³⁴

$$\kappa \nabla^2 T_{\text{ns}} + I / \tau_L = \rho c_p \frac{\partial T_{\text{ns}}}{\partial t} \quad (4)$$

where T_{ns} is the temperature rise in the transient state. The laser intensity I ($\text{W} \cdot \text{m}^{-2}$) is expressed

by

$$I(r, z, t) = I_0 \exp\left(-\frac{r^2}{r_0^2}\right) \exp\left[-4 \ln(2) \frac{t^2}{t_0^2}\right] \exp\left(-\frac{z}{\tau_L}\right) \quad (5)$$

where I_0 ($\text{W}\cdot\text{m}^{-2}$) is the peak laser intensity, t_0 (76 ns) is the pulse width of the ns laser.

Based on Equation (1) and (4), the measured temperature rise of the sample under the two energy transport states are determined by the in-plane thermal conductivity, the laser absorption coefficient and the volumetric heat capacity. By solving Equation (1) and (4), the ratio of the temperature rise of the sample under the two heating states could be obtained. In our experiments, the ratio is equal to the normalized RSC. As the temperature rise caused by laser heating is moderate, ρc_p could be assumed constant. As a result, the ratio could be used to determine the in-plane thermal conductivity of the sample based on the different contribution of heat conduction under the two energy transport states. Note the experimental data (RSC) basically is based on Raman intensity-weighted temperature rise in both time and space. All these are considered in our data processing and detailed later.

The schematic of the Raman system setup for the experiments is shown in Figure 2 (see Methods for more details). Figure 2(c) shows the Raman spectra of two vibrational modes of MoS_2 (E_{2g}^1 and A_{1g}) and one vibration mode of MoSe_2 (A_{1g}) excited by 532 nm laser. The E_{2g}^1 mode of MoS_2 is associated with in-plane opposite vibration of two sulfur atoms with respect to the molybdenum atom, while the A_{1g} modes of the two materials are related to the out-of-plane vibration of only sulfur or selenium atoms in opposite directions.^{24, 35}

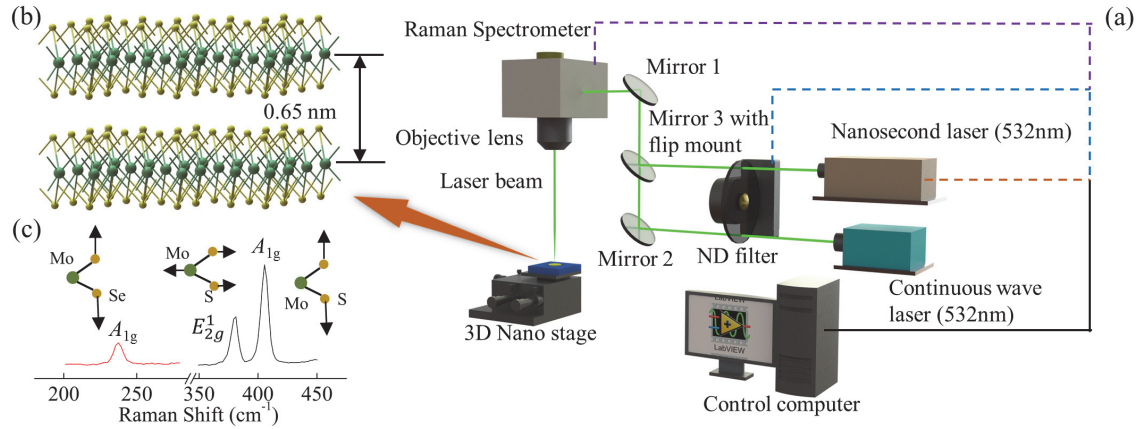


Figure 2. Schematic of the ns ET-Raman system. (a) Suspended 2D atomic-layer sample (MoS_2 or MoSe_2) is irradiated by CW and ns laser. A LabVIEW-based program is used to control the Raman spectrometer and the ND filter. (b) The atomic structure of MoS_2 or MoSe_2 . The green balls are the Mo atoms, and the yellow balls are Sulfur or Selenium atoms. The distance between two adjacent layers is around 0.65 nm. (c) Raman spectra of MoS_2 and MoSe_2 excited by the laser could be used to determine the temperature rise of the sample. E_{2g}^1 ($\sim 383 \text{ cm}^{-1}$) and A_{1g} ($\sim 408 \text{ cm}^{-1}$) modes of MoS_2 , A_{1g} ($\sim 240 \text{ cm}^{-1}$) mode of MoSe_2 are obtained in the experiments. The A_{1g} mode for both MoS_2 and MoSe_2 are used to explore the temperature rise of the samples.

Sample Preparation and Characterization. Four layered MoS_2 samples and four layered MoSe_2 samples are prepared by the mechanical exfoliation method from bulk MoS_2 and bulk MoSe_2 crystals, respectively (see Methods for more details). Compared with samples prepared by chemical vapor deposition and liquid exfoliation, samples with pristine, clean, and high-quality structures could be obtained by using the mechanical exfoliation method.³⁶ Adhesive Scotch tape and gel films (Gel-Film, PF-20/1.5-X4, Gel-Pak) are used to transfer the MoS_2 or MoSe_2 nanosheet to a clean silicon substrate with a hole beneath.³⁷ The hole is fabricated by using the focused ion beam (FIB) technique. The size of the hole is $22 \mu\text{m} \times 22 \mu\text{m}$, and the depth of the hole is $3 \mu\text{m}$. Figure 3 shows the process of sample preparation.

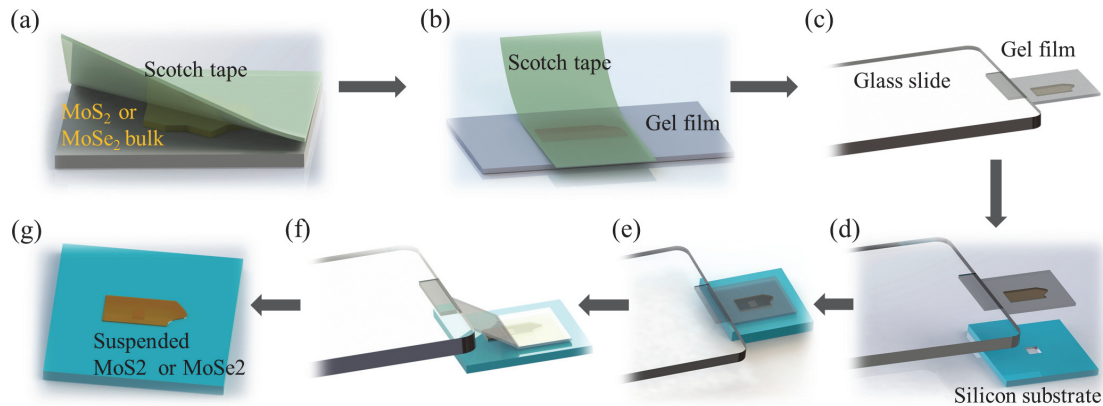


Figure 3. Schematic of the sample preparation process for the Raman experiments. (a) MoS₂ or MoSe₂ are peeled off from the bulk materials using the mechanical exfoliation method. (b) The exfoliated material is then transferred from the scotch tape to a gel film. (c) The gel film is attached to the edge of the glass slide. (d) Align the gel film with the hole in the silicon substrate by using two 3D nano-stages. (e) The gel film is then moved down to touch the silicon substrate. (f) The gel film is moved up slowly to realize the transfer of the sample to the silicon substrate. (g) The obtained suspended MoS₂ or MoSe₂ on silicon substrate.

Figure 4(a) - (h) show the AFM images of the four MoS₂ samples and four MoSe₂ samples. To avoid sample damage, the supported areas of these samples are used to measure the thickness of the samples. In these images, the red dashed lines indicate the thickness profiles shown below. The thickness of MoS₂ samples are 45, 81, 102, and 115 nm, respectively. And the thickness of MoSe₂ samples are 45, 62, 95, and 140 nm, respectively. The biggest thickness variation (Δl_{\max}) along a line of the sample surface is used to evaluate the surface roughness. As shown in the figures, compared with the thickness of the samples, the values of Δl_{\max} for these samples are

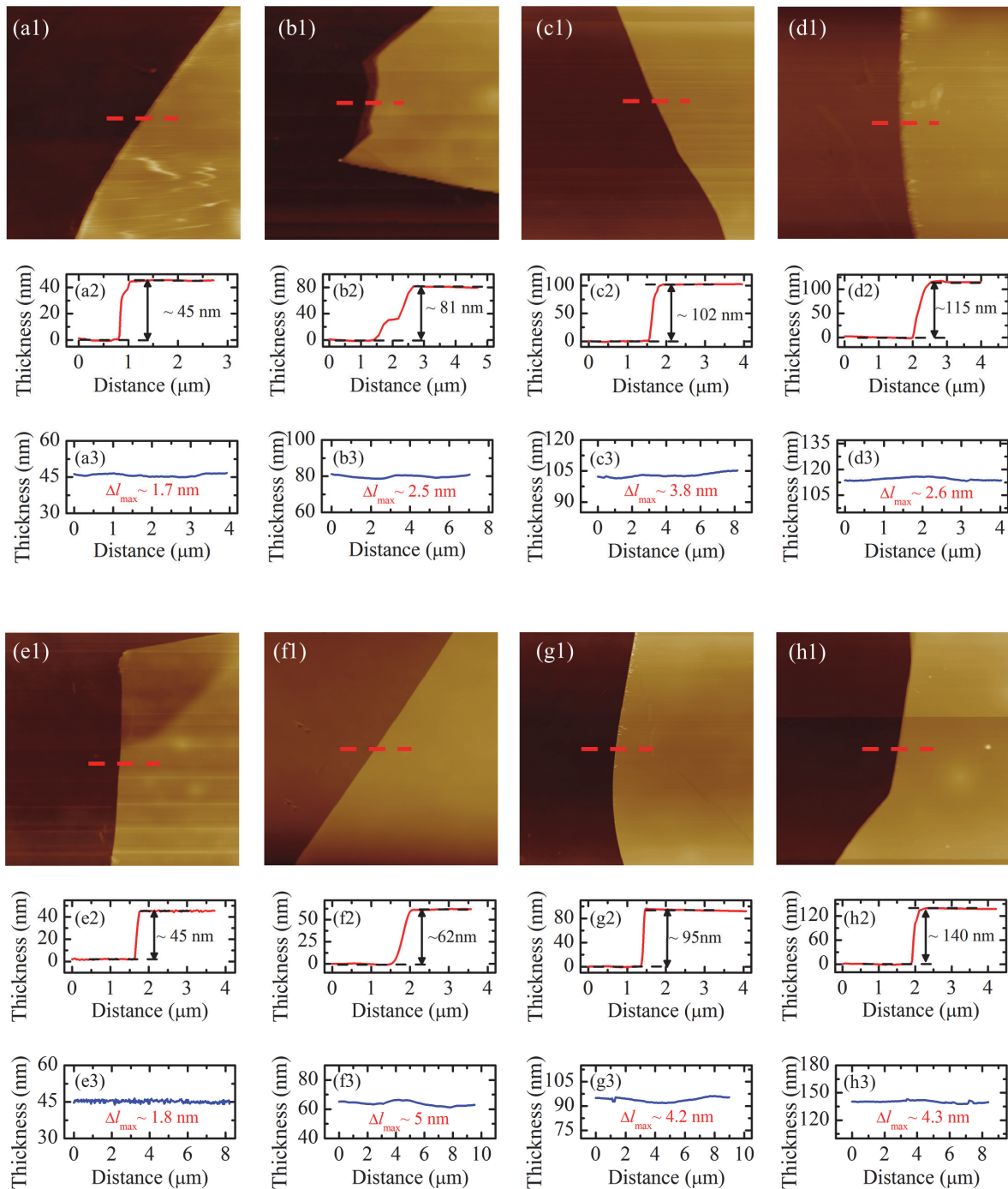


Figure 4. (a-d) AFM measurement results of four suspended MoS₂ samples. (e-h) AFM measurement results of four suspended MoSe₂ samples. (a1-h1) are the AFM images. (a2-h2) are the thickness profiles to show the thickness of the sample corresponding to the red dashed line in the AFM images. (a3-h3) are the thickness profiles to indicate the roughness of the eight samples.

relatively small. And ΔI_{\max} increases with increased thickness. In addition to surface roughness, wrinkles on these samples can also result in the thickness variation. For the 62 nm MoSe₂, ΔI_{\max} is a bit larger which is possibly induced by the not good contact between the sample and substrate in some locations. The root-mean-square roughness (R_q) is also used to reflect the roughness of the samples. For instance, R_q of the four MoS₂ samples are 1.73, 1.95, 2.61, 3.05 nm, respectively. It can be seen that R_q increases a little with increased thickness.

In this work, the nanosecond ET-Raman technique is used to measure these nm-thick MoS₂ and MoSe₂. For a μm -thick sample, this technique is still applicable. However, the temperature distribution in the thickness direction will not be uniform, which means the thermal transport in this direction cannot be neglected. If the thermal conductivity of the material is isotropic, this technique can be used directly. Technique modification is needed if the thermal conductivity of the material is anisotropic. In this case, one more transient state with a different laser heating size is needed. These two transient states can be constructed by using two objectives of different magnification, such as 20 \times and 100 \times . Due to the difference between the two laser heating areas, the contribution of the thermal conductivity in the thickness direction is different in these two states. Combining these two transient states with the steady state, the thermal conductivity of the material in the two directions could be determined. At present, we are using this method to measure the anisotropic thermal conductivity of bulk MoSe₂. Results will be reported in near-future publications.

Thermal response of the sample under CW and ns laser heating. In the Raman experiments, room temperature Raman spectra are collected automatically under different laser power for all

the eight samples to get the Raman shift power coefficient. Both the CW and ns laser power are adjusted based on material and thickness of the sample. For the 45 nm thick MoS₂ sample, the CW laser power is varied from 0.31 mW to 1.82 mW under the 20× objective lens, and the ns laser power is from 0.023 mW to 0.071 mW under the 20× objective lens. The laser power of all the eight samples are listed in Table 1. Note that the laser power here refers to the average power of the laser irradiating the sample surface. The laser power should be maintained as low as possible to avoid sample damage³⁸ and to stay within the linear dependence range of the Raman shift. The diameters of the two laser spots on different samples are also measured. First, the optical images of the laser spots are captured with a CCD (charge-coupled-device) camera (Olympus DP-26, Olympus Optical Co., Ltd.). Then these images are analyzed based on a Gaussian fitting method to calculate the diameters of the laser spots. The obtained values of the diameters (at e^{-1} of the center intensity) of the laser spots on the eight samples are also listed in Table 1. It can be seen that there are some differences among the laser spot on different samples and between the two lasers on the same sample. These differences are induced by the difference between the two lasers, the surface quality of the suspended samples, as well slight variation of the focusing level during the experiment. As the nanosecond ET-Raman technique is based on the assumption of diffusive and local-equilibrium thermal transport, it is necessary to compare the laser spot size with the phonon mean free path (MFP) of the sample. For the high end, the phonon MFP of graphene is about 600 nm³⁹ and the modal MFP of some flexural acoustic (ZA) modes can be several microns.⁴⁰ This is much longer than that of other materials. The phonon mean free path of MoS₂ or MoSe₂ is much shorter. The diameter of the laser spot sizes in our work is about 2.4 μm or larger. That is, the laser spot sizes of the two transport states are much longer than the phonon mean free path of MoS₂ or MoSe₂. Thus, we can take the thermal

transport as diffusive and local-equilibrium. At present we are using the nanosecond ET-Raman to measure the anisotropic thermal conductivity of graphene paper. Due to the long phonon mean free path of graphene, we already found that when we used a 100× objective lens, non-diffusive and local non-equilibrium transport was detected. This is because the diameter of the laser spot under a 100× objective lens is about 600 nm, comparable to the phonon mean free path of graphene. Results will be reported in near-future publications.

Table 1. Summary of the CW and ns laser power range for the eight samples, and the corresponding laser spot diameters under the two lasers.

Sample thickness (nm)	Sample materials	CW laser power range under 20× objective lens (mW)	ns laser power range under 20× objective lens (mW)	CW laser spot diameter (μm)	ns laser spot diameter (μm)
45	MoS ₂	0.31-1.82	0.023-0.071	3.294	2.509
81	MoS ₂	0.58-3.41	0.019-0.112	3.232	2.423
102	MoS ₂	0.67-3.29	0.046-0.178	3.251	2.492
115	MoS ₂	0.67-3.93	0.046-0.178	2.846	2.460
45	MoSe ₂	0.34-1.97	0.046-0.178	3.089	2.471
62	MoSe ₂	0.40-1.95	0.046-0.178	2.843	2.562
95	MoSe ₂	0.44-2.12	0.042-0.200	3.293	2.397
140	MoSe ₂	0.36-1.76	0.042-0.200	3.011	2.400

The 45 nm thick MoS₂ and 45 nm thick MoSe₂ are used to explain the results. Figure 5(a) and (b) show the 3D contour maps of the MoS₂ Raman peaks at 380 cm⁻¹ and 405 cm⁻¹ under different laser powers of the two lasers to give an overall picture on how the Raman intensity of the two peaks varies with the laser power. That is, Raman intensity increases linearly with the increase of laser power. As shown in Figure 5(a), the linearity at some data points are not very good, which

may be induced by the Gaussian fitting errors of the Raman spectra. This could also be caused by the laser heating effect. With the laser irradiating the sample, the local temperature will increase, and the detected Raman intensity will decrease. Figure 5(c) and (d) are also the contour maps of the two Raman peaks to indicate that the two Raman peaks will be redshifted with the increase of laser power. Five representative room temperature Raman spectra of MoS₂ under CW laser and ns laser are shown in Figure 6(a) and (b), respectively. It can also be seen that both the Raman peaks of MoS₂ are red-shifted with the increased laser power. This indicates the local

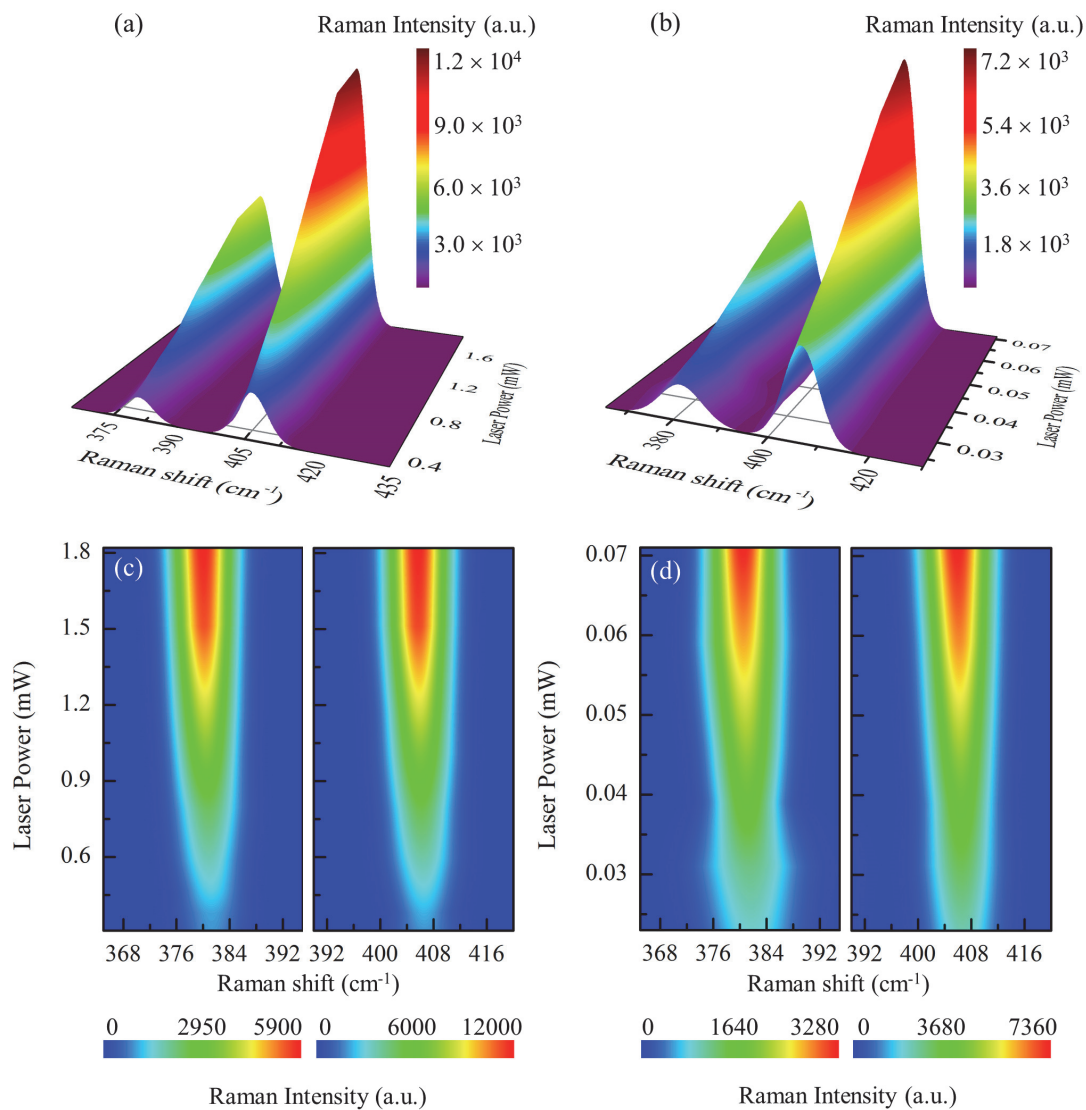


Figure 5. Contour maps of MoS₂ Raman peaks. The 45 nm-thick sample is used to illustrate the ns ET-Raman experimental results. Both a CW laser and a ns laser are used to generate different energy transport states. (a) and (b) are the 3D contour maps to demonstrate the variation of Raman intensity against laser power of CW laser and ns laser, respectively. (c) and (d) are the 2D contour maps to demonstrate the variation of Raman shift against laser power of CW laser and ns laser, respectively.

temperature of the sample is increasing with the increase of laser power. We show the power-dependent peak positions in the linear, low-power range by using $\Delta\omega = \omega(P_2) - \omega(P_1) = \psi(P_2 - P_1) = \psi\Delta P$. As shown in Figure 6(c) and (d), the positions of the

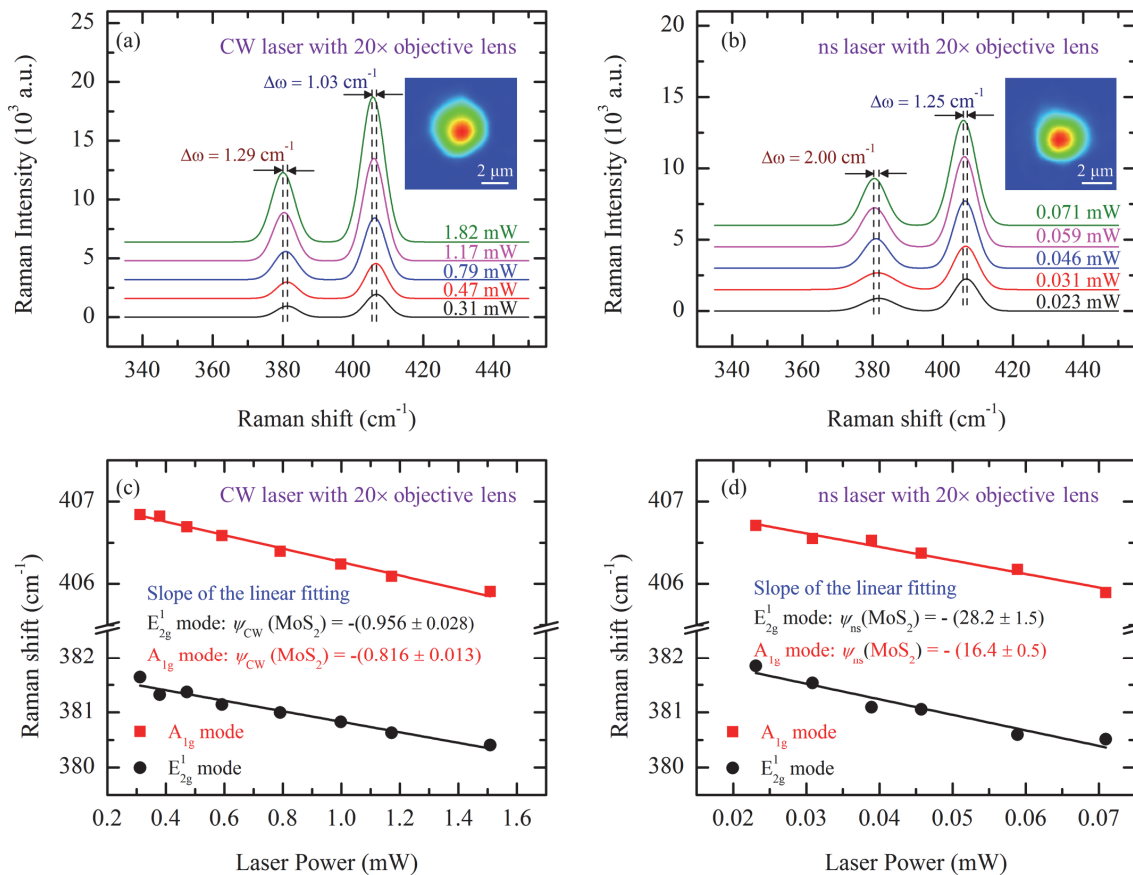


Figure 6. Raman spectra of 45nm-thick suspended MoS₂. (a) Five representative Raman spectra of MoS₂ with increased laser power under CW laser with 20× objective lens in Room Temperature. The variation of Raman shifts for the two modes of MoS₂ are 1.29 cm⁻¹ and 1.03 cm⁻¹, respectively. (b) Five representative Raman spectra of MoS₂ with increased laser power

under ns laser with 20× objective lens in Room Temperature. The variation of Raman shifts for the two modes of MoS₂ are 2.00 cm⁻¹ and 1.25 cm⁻¹, respectively. The spots of the two lasers are also shown in Fig. (a) and (b). For the two lasers, the Raman shifts of the two modes as a function of laser power are shown in Fig. (c) and (d), respectively. The solid lines in the two figures are the fitting results to obtain the linear power coefficient.

two peaks of MoS₂ have a good linear relationship with the laser power. In this work, the A_{1g} mode of MoS₂ is chosen to deduce RSC since E_{2g}¹ mode is prone to strain while A_{1g} is not.⁴¹ It can be seen in Figure 6(c) and (d), the linear fitting results RSC of A_{1g} mode under CW laser is – (0.816 ± 0.013) cm⁻¹/mW, and under ns laser is – (16.4 ± 0.5) cm⁻¹/mW. When the average energy input of the two lasers is the same, the pulse power of the ns laser will be very high, and the thermal diffusion length under ns laser is also much smaller than under CW laser. As a result, the temperature rise of the sample irradiated by ns laser will be much higher than CW laser, and the RSC values under ns laser will also be much larger than that under CW laser.

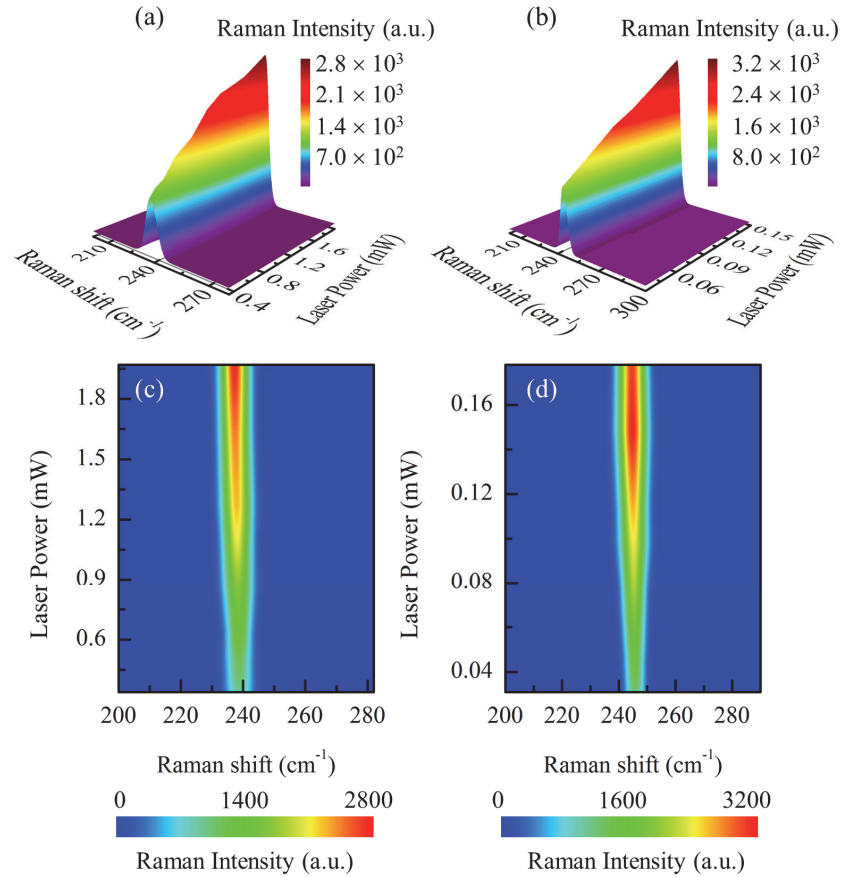


Figure 7. Contour maps of MoSe₂ Raman peak. The 45 nm-thick sample is used to illustrate the ns ET-Raman experimental results. (a) and (b) are the 3D contour maps to demonstrate the variation of Raman intensity against laser power of CW laser and ns laser, respectively. (c) and (d) are the 2D contour maps to demonstrate the variation of Raman shift against laser power of CW laser and ns laser, respectively.

Figure 7(a) and (b) show the 3D contour maps of the MoSe₂ Raman peak at ~240 cm⁻¹ under different laser powers of the two different lasers. The Raman intensity of this peak is also linearly related to the laser power. Figure 7(c) and (d) are contour maps of this Raman peak to show that the peak will also be redshifted with the increase of laser power. Five representative room temperature Raman spectra under the two lasers are also shown in Figure 8(a) and (b). A redshift of the Raman peak could also be seen. It can be seen in Figure 8(c) and (d), the shift of

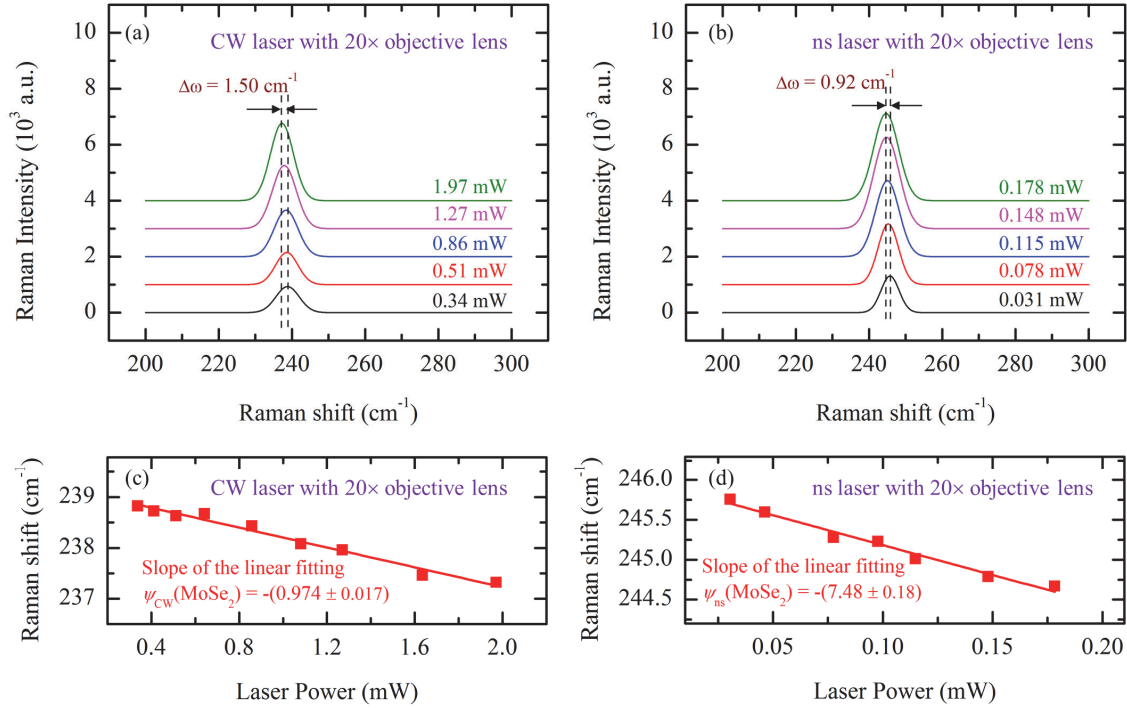


Figure 8. Raman spectra of 45 nm-thick suspended MoSe₂. (a) Five representative Raman spectra of MoSe₂ with increased laser power under CW laser with 20× objective lens in Room Temperature. The variation of Raman shift of MoSe₂ is 1.50 cm⁻¹. (b) Five representative Raman spectra of MoSe₂ with increased laser power under ns laser with 20× objective lens in Room Temperature. The variation of Raman shift of MoSe₂ is 0.92 cm⁻¹. For the two lasers, the Raman shift as a function of laser power are shown in Fig. (c) and (d), respectively. The solid lines in the two figures are the fitting results to obtain the linear power coefficient.

the peak of MoSe₂ is also linearly related to the laser power. The linear fitting results RSC of A_{1g} mode under CW laser is $-(0.974 \pm 0.017) \text{ cm}^{-1}/\text{mW}$, and under ns laser is $-(7.48 \pm 0.18) \text{ cm}^{-1}/\text{mW}$. The RSC values for all the eight samples are listed in Table 2. The RSC values roughly decrease with increased thickness of the samples for both CW and ns laser heating, which indicates that the increase of the in-plane thermal conductance of the sample versus the sample thickness. As the thickness of all the samples are larger than the laser absorption depth of the corresponding materials, the absorbed energy will be nearly the same for samples with different thickness. However, the temperature rise is decreasing, which means that the

temperature rise is smaller for thicker samples. For thicker samples, in-plane thermal conductance is larger due to the larger heat conduction cross-section. As a result, the temperature rise will be smaller for thicker samples.

Determination of thermal conductivity. By combining these two RSC values of CW and ns lasers, a normalized RSC (Θ) is obtained, and the values of the eight samples are also summarized in Table 2. These values listed in Table 2 indicate that Θ increases with increased thickness of MoS₂ and MoSe₂. Then a 3D numerical modeling based on the finite volume method is conducted to calculate the temperature rise under the two energy transport states to determine the in-plane thermal conductivity of MoS₂ and MoSe₂ with different thickness. Figure 9 (a) and (b) show the 3D numerical modeling process under the steady state and the transient state, respectively. The laser power used in the simulation is also very low (0.05 mW) to ensure a small temperature rise. The corresponding laser spot size measured in the experiment is also used in the simulation to guarantee the simulation accuracy. A Raman intensity weighted average temperature over space ($\bar{T}_{CW}|_{\text{Theoretical}}$) under steady state and a Raman intensity weighted average temperature over space and time ($\bar{T}_{ns}|_{\text{Theoretical}}$) under transient state are obtained. This simulation process is done for different κ values. Then the ratios of these two values: $\Theta|_{\text{Theoretical}} = \left((\bar{T}_{ns}|_{\text{Theoretical}} - 22) / (\bar{T}_{CW}|_{\text{Theoretical}} - 22) \right)$ under different trial κ values are used to determine the theoretical curve of Θ against κ . Here “22” is the initial temperature of the sample.

Table 2. Summary of the A_{1g} mode RSC values under the two lasers for the eight samples

Sample thickness (nm)	Sample materials	A_{1g} mode RSC under CW laser (cm^{-1}/mW)	A_{1g} mode RSC under ns laser (cm^{-1}/mW)	Normalized RSC
45	MoS ₂	- (0.816 ± 0.013)	- (16.4 ± 0.5)	20.09 ± 0.69
81	MoS ₂	- (0.322 ± 0.007)	- (8.36 ± 0.19)	25.98 ± 0.82
102	MoS ₂	- (0.299 ± 0.004)	- (8.12 ± 0.15)	27.17 ± 0.62
115	MoS ₂	- (0.268 ± 0.005)	- (7.44 ± 0.10)	27.73 ± 0.64
45	MoSe ₂	- (0.974 ± 0.017)	- (7.48 ± 0.18)	7.68 ± 0.23
62	MoSe ₂	- (0.876 ± 0.014)	- (7.75 ± 0.18)	8.84 ± 0.25
95	MoSe ₂	- (0.553 ± 0.009)	- (6.20 ± 0.13)	11.22 ± 0.30
140	MoSe ₂	- (0.529 ± 0.011)	- (6.95 ± 0.19)	13.15 ± 0.45

Figure 10(a) and (b) show the temperature rise of 45 nm-thick MoS₂ and 45 nm-thick MoSe₂ under the two energy transport states in our modeling. Figure 10(c) and (d) show the theoretical Θ curves of these two samples. And the values obtained in the experiments could be interpolated to determine κ of the samples. As shown in these two figures, the κ values of 45 nm-thick MoS₂ and 45 nm-thick MoSe₂ are 40.0 ± 2.2 , and $11.1 \pm 0.4 \text{ W}\cdot\text{m}^{-1}\cdot\text{K}^{-1}$, respectively. Also, the final results and the uncertainty for the other six samples are summarized in Table 3. In this work, ρc_p and κ are assumed to be constant. Here the 45 nm-thick MoS₂ sample is used to justify this assumption. The Raman shift change ($\Delta\omega$) of this sample under laser irradiation is 0.98 cm^{-1} in CW case. The Raman temperature coefficient (η) is around $0.0123 \text{ cm}^{-1}\cdot\text{K}^{-1}$.²⁸ Then the temperature rise of the sample under laser spot can be calculated as $\bar{T}_{\text{Ra}} = \Delta\omega/\eta = 80 \text{ K}$. The thermophysical properties of the sample are determined by the average temperature rise of the entire sample. This temperature rise can be calculated as $\bar{T}_s = \int 2\pi r T dr / (\pi r_0^2)$, where r is the

distance to the sample's middle point. Using these two values and the theoretical Raman intensity weighted temperature $\bar{T}_{CW}|_{\text{Theoretical}}$ that is shown in Figure 9(a), the average temperature rise of the sample in all domain is determined based on $\bar{T}_{sa} = \bar{T}_s \cdot \bar{T}_{Ra} / (\bar{T}_{CW}|_{\text{Theoretical}} - 22)$. The obtained \bar{T}_{sa} is about 25 K, which is small enough to assume that κ is constant for the experiment. Also, as shown in Figure 6(c) and (d), the Raman shift change of the ns case is close to the CW case. Therefore, the average temperature rise for the ns case is also close to the CW case. As a result, ρc_p can also be assumed constant during the thermal characterization.

As shown in Table 3, the measured in-plane thermal conductivity of suspended MoS₂ films and suspended MoSe₂ films increases with increased film thickness. For MoS₂, when the thickness increases from 45 nm to 115 nm, the corresponding thermal conductivity increases from 40.0 ± 2.2 to 74.3 ± 3.2 W·m⁻¹·K⁻¹.

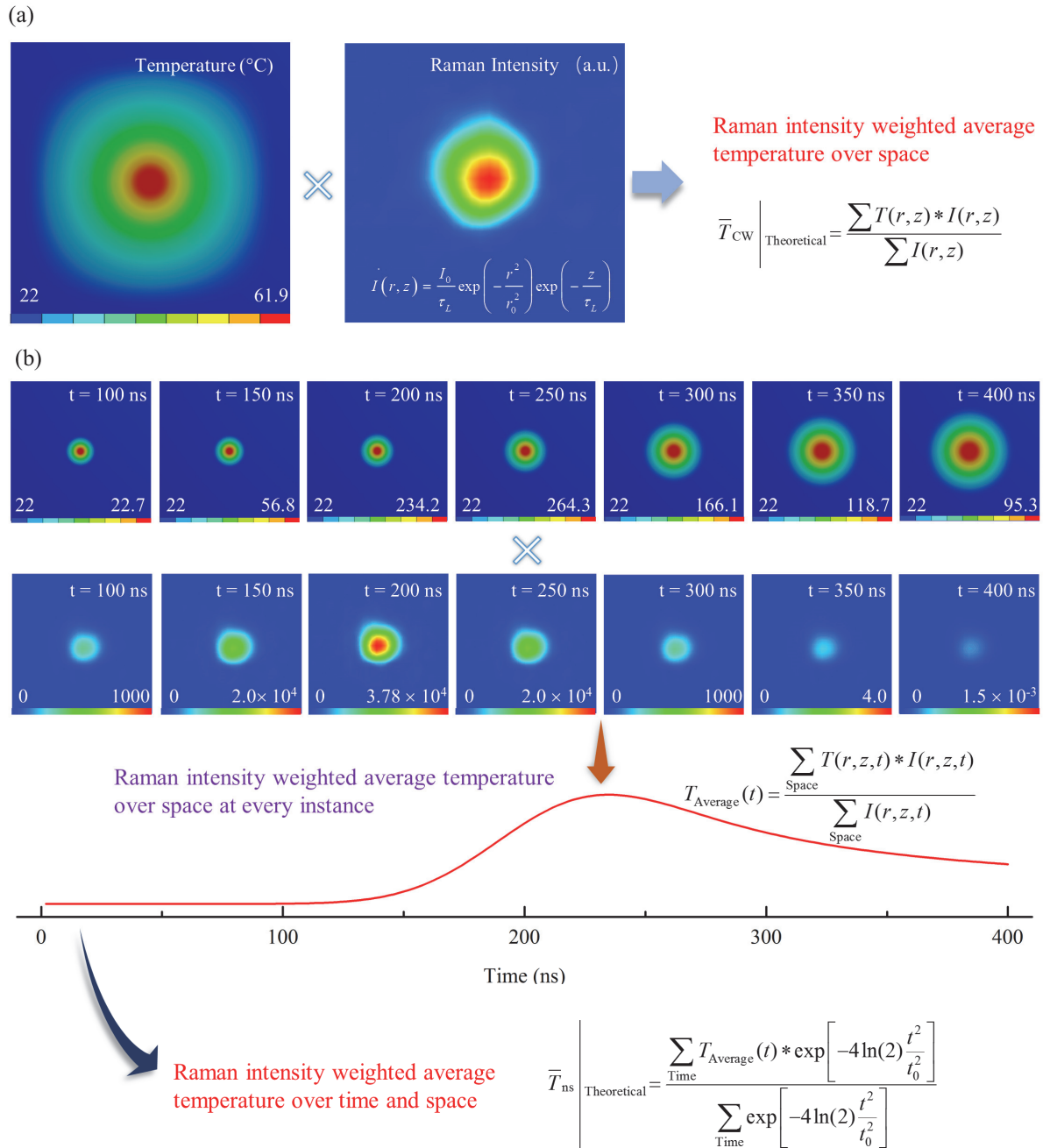


Figure 9. 3D numerical modeling process of ns ET-Raman. (a) Simulation of the heat conduction under CW laser, a Raman intensity weighted average temperature over space domain is obtained based on the temperature and Raman intensity distribution in the space domain. (b) Simulation of the heat conduction under ns laser, a Raman intensity weighted average temperature over time and space domain is obtained based on the temperature and Raman intensity distribution in the time and space domain.

The thermal conductivity of 115 nm-thickness MoS₂ is about 86% higher than the 45 nm-

thickness MoS₂. For MoSe₂, when the thickness increases from 45 nm to 140 nm, the corresponding thermal conductivity increases from 11.1 ± 0.4 to 20.3 ± 0.9 W·m⁻¹·K⁻¹. The thermal conductivity of 140 nm-thickness MoSe₂ is about 83% higher than the 45 nm-thickness MoSe₂. To explore the relationship between the in-plane thermal conductivity and the thickness of these two materials, the thermal conductivity of different thickness obtained in our work and the previously studies is summarized in Figure 11 (a) and (b).^{24, 25, 28, 41-49}

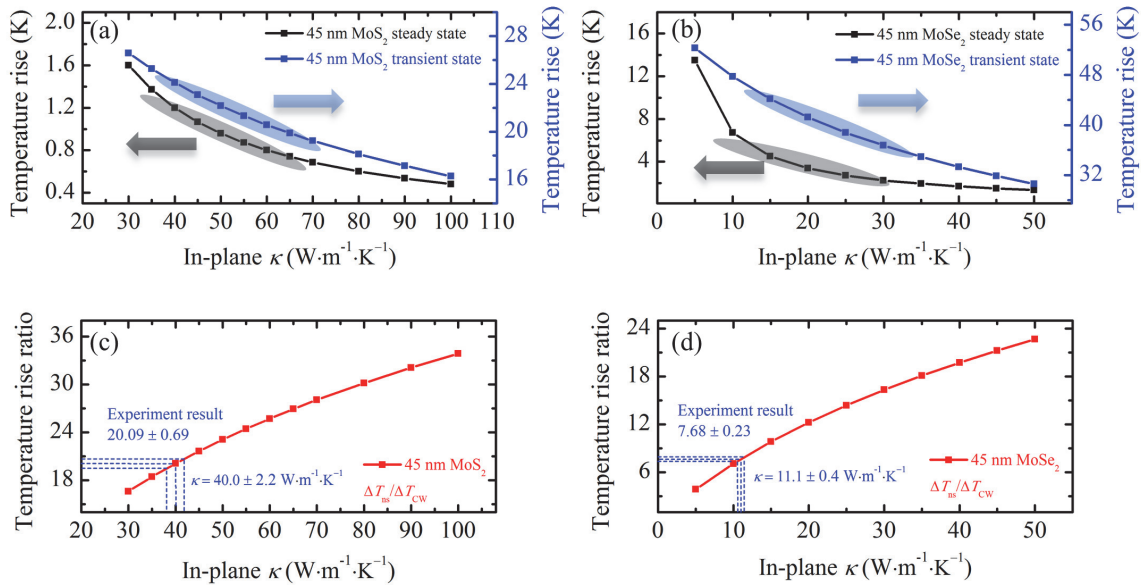


Figure 10. 3D numerical modeling results for the 45 nm thick MoS₂ sample and the 45 nm thick MoSe₂ sample. (a) and (b) show the average temperature rise of MoS₂ and MoSe₂ under the two energy transport states with the increased in-plane thermal conductivity, respectively. (c) and (d) show the relation between the ratio of temperature rise under two energy transport states and the in-plane thermal conductivity of the samples. The in-plane thermal conductivity of the samples is obtained by interpolating the modeling results based on the experimental data.

As shown in these two figures, different values of thermal conductivity for the samples with the same number of layers are observed. The difference can be attributed to three factors. First, the quality of the prepared samples and the measurement methods are different.⁴¹ For atomic-layer

materials, the influence of the surface roughness and the wrinkles on the thermal conductivity could not be neglected. As the disadvantages of different measurement methods could induce different errors, the measured thermal conductivity could also be different. Second, the discrepancy of the obtained temperature coefficients of the samples using temperature-dependent Raman spectroscopy exists in the reported work. This discrepancy is possibly related to the different strain effects on samples with different sizes. Third, the laser absorption coefficient is a very important parameter in the widely used optothermal method based on Raman spectroscopy. However, the coefficient used in different papers is not the same. There can be about 57% difference among these values.²⁵ As a result, the measured thermal conductivity can also be varied significantly.

Table 3. Summary of the in-plane thermal conductivity (κ) determined based on the 3D numerical modeling and experiments

Sample thickness (nm)	Sample materials	κ ($\text{W}\cdot\text{m}^{-1}\cdot\text{K}^{-1}$)	Sample thickness (nm)	Sample materials	κ ($\text{W}\cdot\text{m}^{-1}\cdot\text{K}^{-1}$)
45	MoS ₂	40.0 ± 2.2	45	MoSe ₂	11.1 ± 0.4
81	MoS ₂	57.7 ± 3.2	62	MoSe ₂	14.9 ± 0.5
102	MoS ₂	65.8 ± 2.7	95	MoSe ₂	16.0 ± 0.6
115	MoS ₂	74.3 ± 3.2	140	MoSe ₂	20.3 ± 0.9

As shown in Figure 11(a) and (b), when thickness of the samples is less than 3 nm, there is a trend of decreasing in-plane thermal conductivity with the increased thickness. This is related to the following two factors. The first one is the change in phonon dispersion.⁵⁰ For monolayer MoS₂ or MoSe₂, there are three acoustic branches, including longitudinal acoustic (LA) branch, transverse acoustic (TA) branch, and ZA branch. For few-layered MoS₂ or MoSe₂ ($N \leq 4$), there

are $3N-3$ low-frequency optical phonon branches in addition to the three acoustic branches. A phenomenon named avoided-crossing, which reduces the average group velocity for the heat carrying phonons, could be observed among the optical phonon branches. The thermal conductivity decreases due to the lower group velocity. However, due to the low density and small velocity of the optical phonons, the effect of this factor is quite limited. The other factor is Umklapp scattering resulting from crystal anharmonicity.²⁵

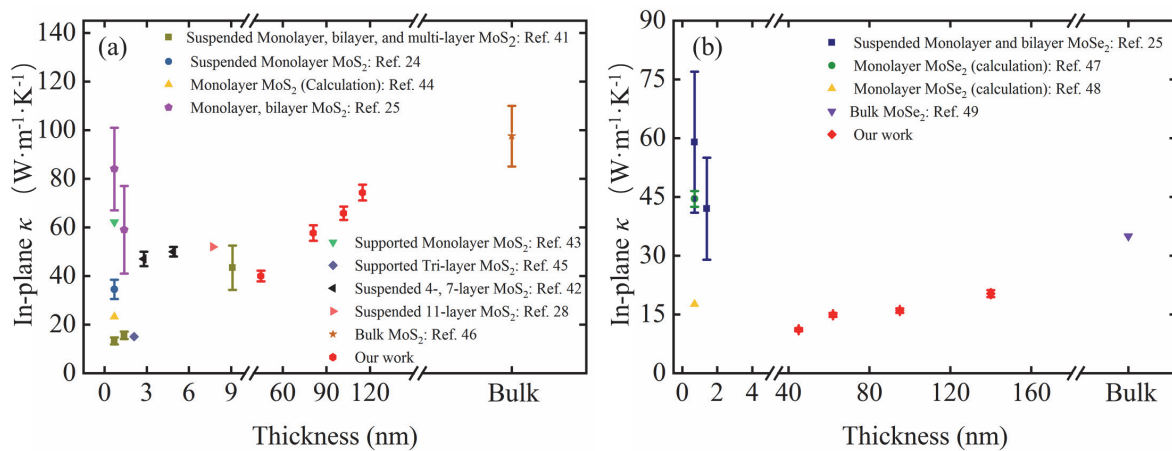


Figure 11. (a) Summary of the in-plane thermal conductivity for the MoS_2 films in this study with that of previously studies. (b) Summary of the in-plane thermal conductivity for the MoSe_2 films in this study with that of previously studies.

In monolayer MoS_2 or MoSe_2 , Umklapp scattering is quenched and the thermal conductivity is affected mostly by the edge boundary scattering. In few-layered samples, the scattering rates of ZA phonons are significantly larger, which means Umklapp scattering plays a much more important role in deterring the thermal conductivity of the samples. For thicker samples, the trend of increasing in-plane thermal conductivity with the increased thickness is clearly observed for both the suspended MoS_2 films and the suspended MoSe_2 films. The thickness dependence of MoS_2 and MoSe_2 originates from significant surface scattering of long mean free path (long-

MFP) phonons. Similar results have been observed in few-layered black phosphorus²³ and few-quintuple-layered Bi₂Te₃ films⁵¹, where surface scattering was found to heavily affect electron and phonon transport.

The surface scattering effect of phonons is analyzed below to explain the thickness-dependent thermal conductivity. By solving the phonon Boltzmann equation using the Landauer approach, the thermal conductivity could be expressed as^{23, 51, 52}

$$\kappa = K_0 \int M_{ph}(\varepsilon) \lambda_{ph}(\varepsilon, T) W_{ph}(\varepsilon, T) d\varepsilon \quad (6)$$

where $K_0 = \pi^2 k_B T / 3h$ is the quantum of thermal conductance, M_{ph} is the number of conducting modes per cross-sectional area, λ_{ph} is the phonon MFP for backscattering, which includes Umklapp phonon-phonon scattering and surface scattering. $W_{ph}(\varepsilon, T) = (3\varepsilon / \pi^2 k_B^2 T) [\partial n_{BE}(\varepsilon, T) / \partial T]$ is a normalized ‘window function’ with n_{BE} being the Bose-Einstein distribution and ε the phonon energy. In our work, the experiments are conducted at room temperature, and the laser heating effect is also very moderate. The phonon dispersion is also nearly the same for samples with different thickness. Conclusively, the effects of $M_{ph}(\varepsilon)$ and $W_{ph}(\varepsilon, T)$ could be neglected. Only the effect of λ_{ph} should be considered. The MFP for MoS₂ and MoSe₂ films is obtained by including the effect of surface scattering using the Fuchs-Sondheimer approach^{51, 52}

$$\lambda_{ph}(E) = \lambda_{bulk} \left[1 - \frac{3(1-p)}{2\delta} \int_1^\infty \left(\frac{1}{x^3} - \frac{1}{x^5} \right) \frac{1-e^{-\delta x}}{1-pe^{-\delta x}} dx \right] \quad (7)$$

where $\delta = (4/3)t / \lambda_{bulk}$, t is the thickness of the film and p is the specular parameter controlling the degree of resistive scattering at the surface, with $p = 0$ and 1 corresponding to

completely diffuse and specular scattering, respectively. Based on Equation (7), the MFP is longer for thicker films, which means less surface scattering effect for thicker films. As a result, the corresponding in-plane thermal conductivity is also higher for thicker films.

▪ Conclusion

A novel technique, entitled ns ET-Raman, was developed to measure the in-plane thermal conductivity (κ) of suspended 2D atomic-layer MoS₂ and MoSe₂ with different thicknesses. A continuous wave laser and a nanosecond pulsed laser were applied to heat and excite the Raman signal. The resulting temperature rise, which were related to κ of the sample, are measured by power differential of Raman shift under the two energy transport states. Due to the different thermal diffusion lengths under the two energy transport states, κ was determined by the ratio of the two Raman shift power coefficients without knowing the laser absorption and temperature coefficients of MoS₂ and MoSe₂. κ was observed to increase with the thickness of both MoS₂ and MoSe₂. For MoS₂, κ increased from 40.0 ± 2.2 to 74.3 ± 3.2 W·m⁻¹·K⁻¹. For MoSe₂, κ increased from 11.1 ± 0.4 to 20.3 ± 0.9 W·m⁻¹·K⁻¹. This thickness dependence was interpreted by the increased significance of surface phonon scattering in thinner samples. ns ET-Raman could also be used to determine the thermal conductivity of other 2D materials with high accuracy and confidence.

▪ Methods

Layered MoS₂ and MoSe₂ Sample Preparation. We prepare four layered MoS₂ samples and four layered MoSe₂ samples by the mechanical exfoliation method from bulk MoS₂ and bulk MoSe₂ crystals, respectively. First, MoS₂ or MoSe₂ are peeled off from the corresponding bulk

materials using the adhesive Scotch tape. The obtained MoS₂ or MoSe₂ on the tapes are then transferred to the gel films. The gel films and the silicon substrate with a hole in the middle are attached to two glass slides, respectively. Two 3D nano stages are used to realize the alignment of the sample on gel film and the hole in the silicon substrate. Then, the gel film is brought in contact with the substrate and pressed gently. The sample is transferred to the hole area on the silicon substrate when the gel film is slowly moved away from the silicon substrate. The obtained suspended samples are identified by using an optical microscope, and atomic force microscope (AFM) (NMAFM-2, Digital Instruments, CA, USA).

Experimental Details. The Raman experiments are conducted by using a confocal Raman system, which is shown in Figure 2(a). This system consists of a Raman spectrometer (Voyage, B&W Tek, Inc.) and a microscope (Olympus BX53). A CW laser (Excelsior, Spectra-Physics) or ns laser (DCL AIO Laser, Photonics Industries, International, Inc.) with the same wavelength (532 nm) is introduced to the system, and a motorized neutral-density (ND) filter (CONEX-NSR, Newport Corporation) is used to adjust the laser power. The switch of the two lasers could be realized by a flip mirror without any other change to the system setup.

During the experiment, the Raman spectrometer and the ND filter are controlled by a LabVIEW-based software to realize automatic acquisition and saving of the Raman spectra, and automatic adjustment of the ND filter. At the same time, the experiment time is shortened significantly, the environmental interference to the system is reduced, and the accuracy of the experiment is improved dramatically. In the experiment, a 20× objective lens (NA=0.4) is used for the two energy transport states. RSC of the sample under the two energy transport states could be

obtained based on the acquired Raman spectra. For the steady-state heating, the influence of hot carrier transfer on the measured RSC are much smaller by using the 20× objective lens than using objective lens with a higher magnification. That is, the influence of hot carrier transfer is related to the laser spot size. The hot carrier diffusion length is around 0.4 μm for MoS₂, which is much smaller than the laser spot size under 20× objective lens (around 3 μm).²¹ As a result, the effect of hot carrier transfer becomes more negligible. For the transient-state heating, the energy density of the ns laser is very high. The larger magnification of the objective lens, the higher the energy density of the laser on the sample. The sample will be damaged when the energy density is too high. As a result, the 20× objective lens is used. Then, RSC of the sample under the two energy transport states could be obtained based on the acquired Raman spectra to determine the in-plane thermal conductivity of the sample.

Author Information

Corresponding Author

*E-mail: xx_xs316@163.com (S.X), xwang3@iastate.edu (X.W)

Present Address

Shen Xu: Automotive Engineering College, Shanghai University of Engineering Science, 333 Longteng Road, Shanghai 201620, People's Republic of China.

Xinwei Wang: 271 Applied Science Complex II, Department of Mechanical Engineering, Iowa State University, Ames, IA 50011, United States.

Acknowledgements

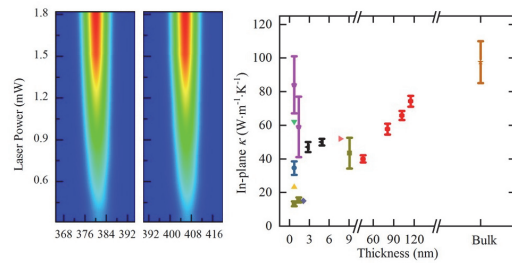
Support of this work by National Science Foundation (CBET1235852, CMMI1264399) and Department of Energy (DENE0000671) is gratefully acknowledged.

References

1. G. Fugallo, A. Cepellotti, L. Paulatto, M. Lazzeri, N. Marzari and F. Mauri, *Nano Lett*, 2014, **14**, 6109-6114.
2. M. Han, P. Yuan, J. Liu, S. Si, X. Zhao, Y. Yue, X. Wang and X. Xiao, *Sci Rep*, 2017, **7**, 12213.
3. A. Gupta, T. Sakthivel and S. Seal, *Progress in Materials Science*, 2015, **73**, 44-126.
4. X. Ling, S. Huang, E. H. Hasdeo, L. Liang, W. M. Parkin, Y. Tatsumi, A. R. Nugraha, A. A. Poretzky, P. M. Das, B. G. Sumpter, D. B. Geohegan, J. Kong, R. Saito, M. Drndic, V. Meunier and M. S. Dresselhaus, *Nano Lett*, 2016, **16**, 2260-2267.
5. T. Wang, J. Liu, B. Xu, R. Wang, P. Yuan, M. Han, S. Xu, Y. Xie, Y. Wu and X. Wang, *Chemphyschem*, 2017, **18**, 2828-2834.
6. R. Ganatra and Q. Zhang, *Acs Nano*, 2014, **8**, 4074-4099.
7. S. Larentis, B. Fallahazad and E. Tutuc, *Appl Phys Lett*, 2012, **101**, 223104.
8. B. M. Nichols, A. L. Mazzoni, M. L. Chin, P. B. Shah, S. Najmaei, R. A. Burke and M. Dubey, 2016, **95**, 221-277.
9. A. B. Kaul, *Journal of Materials Research*, 2014, **29**, 348-361.
10. E. Yalon, C. J. McClellan, K. K. H. Smithe, M. Munoz Rojo, R. L. Xu, S. V. Suryavanshi, A. J. Gabourie, C. M. Neumann, F. Xiong, A. B. Farimani and E. Pop, *Nano Lett*, 2017, **17**, 3429-3433.
11. I. Jo, M. T. Pettes, J. Kim, K. Watanabe, T. Taniguchi, Z. Yao and L. Shi, *Nano Lett*, 2013, **13**, 550-554.
12. H. Jang, J. D. Wood, C. R. Ryder, M. C. Hersam and D. G. Cahill, *Adv Mater*, 2015, **27**, 8017-8022.
13. A. Aiyiti, X. Bai, J. Wu, X. Xu and B. Li, *Science Bulletin*, 2018.
14. K. M. Shahil and A. A. Balandin, *Nano Lett*, 2012, **12**, 861-867.
15. D. Zhao, X. Qian, X. Gu, S. A. Jajja and R. Yang, *Journal of Electronic Packaging*, 2016, **138**, 040802.
16. J.-U. Lee, M. Kim and H. Cheong, *Applied Microscopy*, 2015, **45**, 126-130.
17. S. Najmaei, Z. Liu, P. M. Ajayan and J. Lou, *Appl Phys Lett*, 2012, **100**, 013106.
18. L. Su and Y. Zhang, *Appl Phys Lett*, 2015, **107**, 071905.
19. H.-D. Wang, J.-H. Liu, X. Zhang and Y. Song, *International Journal of Heat and Mass Transfer*, 2014, **70**, 40-45.
20. A. Aiyiti, S. Hu, C. Wang, Q. Xi, Z. Cheng, M. Xia, Y. Ma, J. Wu, J. Guo, Q. Wang, J. Zhou, J. Chen, X. Xu and B. Li, *Nanoscale*, 2018, **10**, 2727-2734.
21. P. Yuan, J. Liu, R. Wang and X. Wang, *Nanoscale*, 2017, **9**, 6808-6820.
22. J.-U. Lee, D. Yoon, H. Kim, S. W. Lee and H. Cheong, *Phys Rev B*, 2011, **83**, 081419.
23. Z. Luo, J. Maassen, Y. Deng, Y. Du, R. P. Garrelts, M. S. Lundstrom, P. D. Ye and X. Xu, *Nat Commun*, 2015, **6**, 8572.
24. R. Yan, J. R. Simpson, S. Bertolazzi, J. Brivio, M. Watson, X. Wu, A. Kis, T. Luo, A. R. H. Walker and H. G. Xing, *Acs Nano*, 2014, **8**, 986-993.
25. X. Zhang, D. Sun, Y. Li, G. H. Lee, X. Cui, D. Chenet, Y. You, T. F. Heinz and J. C. Hone, *ACS Appl Mater Interfaces*, 2015, **7**, 25923-25929.
26. P. Yuan, R. Wang, H. Tan, T. Wang and X. Wang, *ACS Photonics*, 2017, **4**, 3115-3129.
27. D. J. Late, S. N. Shirodkar, U. V. Waghmare, V. P. Dravid and C. N. Rao, *Chemphyschem*, 2014, **15**, 1592-1598.
28. S. Sahoo, A. P. S. Gaur, M. Ahmadi, M. J. F. Guinel and R. S. Katiyar, *The Journal of Physical Chemistry C*, 2013, **117**, 9042-9047.
29. X. Chen and X. Wang, *The Journal of Physical Chemistry C*, 2011, **115**, 22207-22216.
30. C. Yim, M. O'Brien, N. McEvoy, S. Winters, I. Mirza, J. G. Lunney and G. S. Duesberg, *Appl Phys Lett*, 2014, **104**, 103114.
31. H.-L. Liu, C.-C. Shen, S.-H. Su, C.-L. Hsu, M.-Y. Li and L.-J. Li, *Appl Phys Lett*, 2014, **105**, 201905.
32. C. Christofides, A. Othonos and E. Loizidou, *J Appl Phys*, 2002, **92**, 1280-1285.
33. E. Marin, *Latin-American Journal of Physics Education*, 2010, **4**, 5.

34. S. Sinha, *Ceramics International*, 2015, **41**, 6596-6603.
35. S. K. Balasingam, J. S. Lee and Y. Jun, *Dalton Trans*, 2015, **44**, 15491-15498.
36. H. Li, J. Wu, Z. Yin and H. Zhang, *Accounts of Chemical Research*, 2014, **47**, 1067-1075.
37. A. Castellanos-Gomez, M. Buscema, R. Molenaar, V. Singh, L. Janssen, H. S. J. van der Zant and G. A. Steele, *2D Materials*, 2014, **1**, 011002.
38. E. Mercado, A. Goodyear, J. Moffat, M. Cooke and R. S. Sundaram, *Journal of Physics D: Applied Physics*, 2017, **50**, 184005.
39. E. Pop, V. Varshney and A. K. Roy, *MRS Bulletin*, 2012, **37**, 1273-1281.
40. B. Qiu and X. Ruan, *Applied Physics Letters*, 2012, **100**, 193101.
41. J. J. Bae, H. Y. Jeong, G. H. Han, J. Kim, H. Kim, M. S. Kim, B. H. Moon, S. C. Lim and Y. H. Lee, *Nanoscale*, 2017, **9**, 2541-2547.
42. I. Jo, M. T. Pettes, E. Ou, W. Wu and L. Shi, *Appl Phys Lett*, 2014, **104**, 201902.
43. A. Taube, J. Judek, A. Lapinska and M. Zdrojek, *ACS Appl Mater Interfaces*, 2015, **7**, 5061-5065.
44. Y. Cai, J. Lan, G. Zhang and Y.-W. Zhang, *Phys Rev B*, 2014, **89**.
45. T. S. Sreepasad, P. Nguyen, N. Kim and V. Berry, *Nano Lett*, 2013, **13**, 4434-4441.
46. J. Liu, G.-M. Choi and D. G. Cahill, *J Appl Phys*, 2014, **116**, 233107.
47. Y. Hong, J. Zhang and X. C. Zeng, *The Journal of Physical Chemistry C*, 2016, **120**, 26067-26075.
48. B. Peng, H. Zhang, H. Shao, Y. Xu, X. Zhang and H. ZHu, *Rsc Adv*, 2016, **6**, 5767-5773.
49. P. Jiang, X. Qian, X. Gu and R. Yang, *Adv Mater*, 2017, **29**.
50. X. Gu, B. Li and R. Yang, *J Appl Phys*, 2016, **119**, 085106.
51. M. T. Pettes, J. Maassen, I. Jo, M. S. Lundstrom and L. Shi, *Nano Lett*, 2013, **13**, 5316-5322.
52. C. Jeong, S. Datta and M. Lundstrom, *J Appl Phys*, 2012, **111**, 093708.

Graphical Table of Contents (TOC) entry



Nanosecond ET-Raman measures thermal conductivity of 2D materials without temperature calibration and laser absorption evaluation and features highest accuracy.